Molecular chirality and domain shapes in lipid monolayers on aqueous surfaces

Peter Krüger and Mathias Lösche
Institute of Experimental Physics I, Leipzig University, Linnéstrasse 5, D-04103 Leipzig, Germany
(Received 4 April 2000)

The shapes of domain boundaries in the mesoscopic phase separation of phospholipids in aqueous surface monolayers are analyzed with particular attention to the influence of molecular chirality. We have calculated equilibrium shapes of such boundaries, and show that the concept of spontaneous curvature—derived from an effective pair potential between the chiral molecules—yields an adequate description of the contribution of chirality to the total energy of the system. For enantiomeric dipalmitoylphosphatidylcholine in pure monolayers, and in mixtures with impurities that adsorb preferentially at the (one-dimensional) boundary line between the isotropic and anisotropic fluid phases, such as cyanobiphenyl (5CB), a total energy term that includes line tension, electrostatic dipole-dipole interaction, and spontaneous curvature is sufficient to describe the shapes of well-separated domain boundaries in full detail. As soon as interdomain distances fall below the domain sizes upon compression of a monolayer, fluctuations take over in determining its detailed structural morphology. Using Minkowski measures for the well-studied dimyristoyl phosphatidic acid (DMPA)/cholesterol system, we show that calculations accounting for line tension, electrostatic repulsion, and molecular chirality yield boundary shapes that are of the same topology as the experimentally observed structures. At a fixed molecular area in the phase coexistence region, the DMPA/cholesterol system undergoes an exponential decay of the line tension λ with decreasing subphase temperature T.

PACS number(s): 87.16.Dg, 87.14.Cc, 05.65.+b, 05.70.Fh

I. INTRODUCTION

Langmuir monolayers of amphiphilic molecules at the air-water interface show mesoscopic—i.e. μm scale—structure formation in the course of a first-order phase transition between the isotropic and an anisotropic quasi-two-dimensional (2D) fluid phase [1–3]. Such monomolecular layers are typically prepared in a Langmuir film balance which permits a continuous decrease of the area A per molecule in the film, resulting in a monotonic increase of the lateral pressure on the film, $\pi = \gamma_0 - \gamma$, where γ is surface tension. Since the textures are mesoscopic, it is quite straightforward to observe them using fluorescence microscopy (FM)[1] [4,5]—utilizing the partitioning of an amphiphilic dye between coexisting phases—or Brewster angle microscopy (BAM) [6] which does not introduce a label but is more limited in optical resolution. It has been generally accepted that the sizes and shapes of coexisting phase domains are controlled by the competition of molecular interactions—the (one-dimensional) line tension between the coexisting phases and electrostatic repulsion between excess dipole moments on the condensed phase—where the increased area density of the charged or zwitterionic amphiphiles leads to a dipole moment density that is increased over that of the expanded phase. An analysis of the shapes of phase coexistence textures should thus—in principle—yield a quantitative analysis of the molecular interactions in such films. In this context it is interesting to note that very similar patterns to those previously observed in phospholipid monolayers [7,8] were also recently shown to occur in bilayer leaflets of giant unilamellar vesicles using two-photon fluorescence microscopy [9].

Particularly interesting are domain structures in Langmuir films of biological compounds—such as phospholipids [10,11]. In this context, a quantification of molecular interactions may also bear physiological implications, since the association of, e.g., peripheral proteins with membranes is likely to be sensitive to electrostatic interactions. Moreover, since such lipids are invariably chiral, the mesoscopic structure formation will also be affected by the handedness of the constituent molecules [5,12]. Similar effects were demonstrated for complex, chiral amphiphiles that lack biological relevance [13,14]. In addition, branching of the structures may occur [15–18], and far from equilibrium domain growth is susceptible to diffusion limitation [19], leading to effects similar in nature to constitutional supercooling [20]. Under near-equilibrium conditions, the compression speed dA/dt controls the final size of the domains, since fewer nucleation centers per unit area are formed at low speed than at high speed at the onset of the phase transition [21,22]. Compounds with a large susceptibility for enrichment at the 2D fluid-fluid contact line in the monolayer films—such as cholesterol—are known to reduce the line tension, and lead to an elongation of the structures [12,15,23] due to the relative enhancement of electrostatic repulsion within the domains [12,24]. The sum of these effects leads to a dizzying richness of shapes observed in monomolecular films, which severely complicates any quantitative assessment.

Theory treats these low-dimensional objects as 2D dipolar

[1]Abbreviations: FM, fluorescence microscopy; BAM, Brewster angle microscopy; GIXD, grazing-incidence x-ray diffraction; DPPC, 1,2-dipalmitoyl-glycero-3-phosphatidylcholine; EPP, effective pair potential; DMPA, 1,2-dimyristoyl-glycero-3-phosphatidic acid; DMPE, 1,2-dimyristoyl-glycero-3-phosphatidylethanolamine; NBD-PC, 1-palmitoyl-2-lauroyl-nitrobenzoxadiazol-glycero-3-PC; 5CB, 4-cyano-4′-N-pentylbiphenyl; EDTA, ethylenediamin tetraacetic acid; LE, liquid expanded; LC, liquid condensed.

discs [25,26] that are subject to plastic deformation [15]. Most approaches concentrated on the competition between line tension and electrostatic repulsion [18,24,27], which suffices to describe many essential features of the observed textures. With a few exceptions [28,29], the contribution of molecular chirality to structure formation was recognized [5], but not explicitly taken into account in attempts on a quantitative description. Generally, structure formation has been treated either as an equilibrium problem concerning individual domains [27,30,31] or in terms of thermodynamic properties—e.g., of hexagonal or stripe phases [24,32] and their transitions. No attention was paid so far to the assessment of shapes of domains in the field originating from their neighbors within a monolayer in which crowding of domains occurs—which is the realistic situation for the most part during the phase transition. The reason for this is that under the influence of the variety of factors that govern structure formation, fluctuations lead to a variability of the observed patterns which are similar to each other—but not identical. This complicates a detailed evaluation of the data greatly, and has so far prevented a quantitative comparison with models. Thus the kidney-shaped textures [5,23,33] that are typical of enantiomerically pure phospholipids such as DPPC, DPPG, or DMPA have not yet been reproduced in a static, quasi-equilibrium situation in which they occur (although a kinetic approach has been suggested [28]).

In the work reported here, we introduce a term, based on the concept of spontaneous curvature, that contributes to the free energy of the system, and accounts for the internal structure of the domains. We show that essential features of the structure formation are well described by three components in the free energy—line tension and electrostatic repulsion, as introduced by McConnell and others [24,25], and spontaneous curvature due to long-range accumulation effects of the local molecular chirality. It is demonstrated that this description works well for systems in which elongated domains—that may be treated as quasi-1D structures—are formed at large distances from each other ($d \gg L$, the length of a typical domain), such that domain-domain interactions may be neglected. We then demonstrate that the formalism may also be used to model domain structures in a truly 2D situation, although our implementation is limited to an analysis near the onset of the phase transition where the domains are still well separated. The values determined for spontaneous curvature in that case are compatible with typical correlation lengths for the positional order of molecules in hexatic domains as determined using GIXD [34]. Finally, we use the approach of simulating ensembles of elongated, quasi-1D domains, thus arriving at a situation that permits a comparison of models with the realistic situation in which many domains coexist within the monolayer in close vicinity of each other. As such a comparison is limited to an evaluation of *similarities*—since the detailed shapes of individual domains in a tightly packed regime are governed by fluctuations—we apply integral geometric techniques to characterize morphological measures of the observed and simulated patterns. As an alternate means of comparing experimental and calculated data, we determine the width-to-length ratios of the domains. In such a comparison, a continuous development of the line tension values is observed in simulations that relate to a sequence of images obtained in an experiment in which temperature variation controls the transition from a hexagonal to a striped phase under the influence of molecular chirality [12].

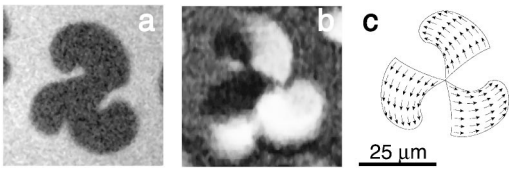

FIG. 1. Domains of L-DPPC on pure water ($T \approx 20\,^{\circ}\mathrm{C}, \pi \approx 9$ mN/m) as visualized with FM (0.5-mol % NBD-PC, left panel) or BAM (center panel). A putative distribution of the director orientations of the tilted chains [40], consistent with the gray level distribution observed in the BAM image, is shown on the right.

II. EXPERIMENT

Chloroform was from Merck (Darmstadt, Germany) and methanol from Sigma-Aldrich (Deisenhofen, Germany). Both were of p.a. grade. The synthetic phospholipids dipalmitoylphosphatidylcholine and dimyristoylphosphatidic acid (L-α-DPPC, D-α-DPPC, and L-α-DMPA), as well as cholesterol, were from Sigma-Aldrich. They were specified 99% + pure, and used as received. NaCl, NaOH, and EDTA were from Sigma-Aldrich (p.a. grade). Cyanopentylbiphenyl (5CB) was from Merck. The chain-labeled fluorescent lipid NBD-PC from Molecular Probes (Leiden, The Netherlands) was used at a concentration of 0.5 mol % with respect to total lipid. Lipids were spread from 3:1 (chloroform:methanol) solutions in concentrations of ≈ 0.5 mg/mL on pure water subphases. The water was filtered using a Milli-Q device (Millipore, Eschborn, Germany), and had a resistivity of > 18 MΩ cm. Both the fluorescence and Brewster angle microscopy setup are of local design [35,36]. Fluorescence microscopy data are directly stored into computer memory (928×640 pixels), and processed using the public domain software NIH Image, v. 1.62 [37] and routines written in the yorick 1.4 programming language [38].

III. RESULTS AND DATA MODELING

A. Chirality of DPPC domains

Phase separated films of enantiomeric DPPC on pure water show that the molecular chirality is expressed in the mesoscopic structure [5]. As typical examples, Fig. 1 shows a micrograph of a L-α-DPPC monolayer [(a): FM at $\pi \approx 9$ mN/m and $A \approx 65$ Å^2 and (b): BAM taken under comparable conditions] in which ordered domains [dark in Fig. (1(a)], embedded in a continuous phase of disordered lipid, have been formed in the course of the first-order liquid expanded–liquid condensed (LE/LC)[2] phase transition. Both images were taken at room temperature ($T = 20 \pm 1\,^{\circ}\mathrm{C}$) and are clippings from a larger field of view. The FM image was observed using 0.5 mol % NBD-PC. Each of the domains [that are not identical in Figs. 1(a) and 1(b)] have grown three lobes from their centers, which curve back on them-

[2]Phospholipid monolayer phases are denoted according to Cadenhead *et al.* [39].

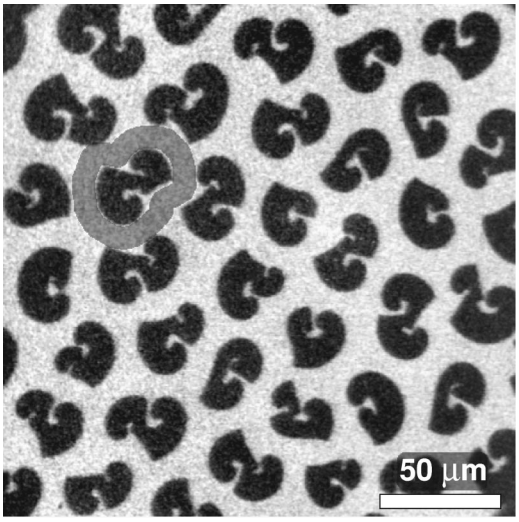

FIG. 2. FM micrograph (0.5-mol % NBD-PC) of a tightly packed ensemble of *L*-DPPC domains in a monolayer on pure water ($T \approx 20\,^{\circ}\mathrm{C}, \pi \approx 9$ mN/m). By highlighting the surrounding of one domain, the ''world map effect'' (cf. footnote in the text) is exemplified.

selves, thus forming the beginnings of left-handed spirals. Neutron and x-ray reflectivity measurements showed that the ordered acyl chains of DPPC in the LC phase are tilted by $\approx 30°$ from the surface normal [40]. Such a tilting of the long molecular axis leads to optical anisotropy which is observed in the BAM image [Fig. 1(b)] as a continuous variation of the brightness level as one follows the long axis of the spiraling lobes. This indicates that the mesoscopic curvature of the dividing line between the coexisting phases is correlated with the local orientation of the tilt azimuth of the acyl chains. A schematic model of the vector field representing these azimuth directions—consistent with the brightness level distribution observed in the BAM image given the direction of the incoming laser beam—is indicated in Fig. 1(c).

Close inspection of Fig. 1 reveals that the curved lobes are not simply bent rectangular shapes. Rather, the domain contours are more complicated, which is particularly obvious in the center section whence the lobes have grown from a common center, the domain nucleus. The contour line in this region reflects clearly the impact of long-range interactions by which outer areas of the domain are repelled by inner areas. Obviously, the detailed shape of such domains may not simply be described using one-dimensional models. This point is stressed by the fluorescence micrograph in Fig. 2, which shows an *L*-α-DPPC monolayer in a state where the LE→LC phase transition has been further driven toward completion ($\pi = 8.9$ mN/m and $A = 65$ Å^2). A remarkably regular array of domains is observed, densely packed within the film area, in which the shapes of the individual domains are all quite similar to each other, mostly showing two lobes although one-lobed domains also frequently occur. Close inspection shows also that no individual contour is identical to any other, which impressively stresses the role of fluctuations. By and large, however, electrostatic long range interactions, i.e., the repulsion of collinearly oriented dipole moments, determine the overall arrangement most significantly. A gray zone overlaid on the image indicates locations where the action of such long-range repulsion has led to a mutual

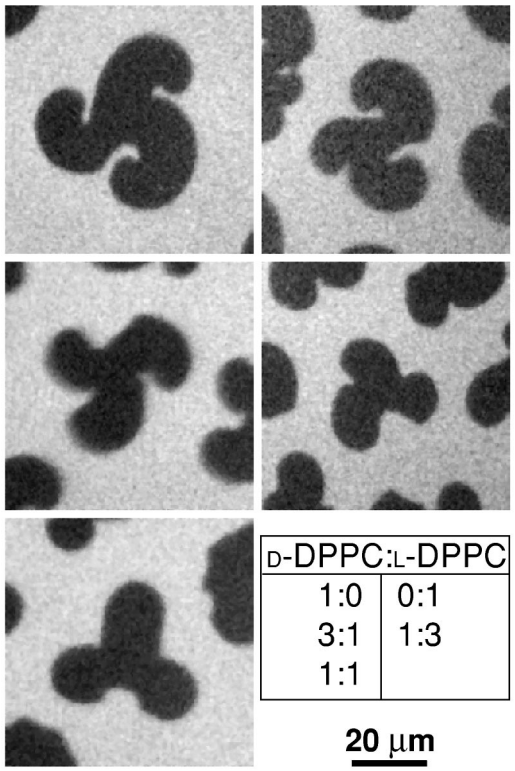

FIG. 3. FM images (0.5-mol % NBD-PC) of mixed monolayers of *L*-DPPC and *D*-DPPC on water ($T \approx 20\,^{\circ}\mathrm{C}, \pi \approx 9$ mN/m) with mixing ratios as indicated.

arrangement of the contour lines of neighboring domains *over a distance of some 10 μm*.[3] We conclude from these images that both intradomain and interdomain electrostatic interactions determine the textures observed in such monolayers.

Figure 3 shows a series of FM images from monolayers incorporating various mixing ratios, *L*-α-DPPC: *D*-α-DPPC, at room temperature and similar π,*A* values (≈ 9 mN/m, 65 Å^2). It is observed that the mesoscopic curvature of the domain lobes is correlated with the enantiomeric constitution of the lipid, and most distinct for the pure components. Upon progressive mixing of the enantiomers, the curvature is gradually reduced, and for the racemate the curvature has entirely vanished.

In order to separate the effect of molecular chirality from other contributions to the Hamiltonian, and to test models describing its impact, it may be advantageous to start with filamentous domains of chiral amphiphiles in which the individual domains are well separated (the interdomain distances are much greater than the domain diameters). While the DPPC/cholesterol [23] or DMPA/cholesterol [12] systems reported on previously meet the first condition, their filamentous domains are so close to each other that interdomain interactions cannot be neglected. We found a similar system, DPPC/5CB, which forms quasi-1D domains that stay

[3]This arrangement might be called the ''world map effect'' because of its close resemblance to the formation of continental contour lines, e.g., on both sides of the Atlantic Ocean due to the continental drift.

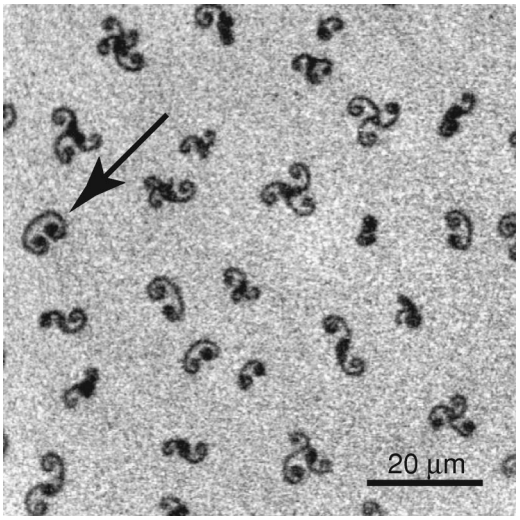

FIG. 4. FM micrograph (0.5 mol % NBD-PC) of a *L*-DPPC monolayer incorporating 19 mol % 5CB on water ($T \approx 20\,^{\circ}\mathrm{C}, \pi \approx 14$ mN/m).

separated within the film thus fulfilling both criteria rather well. Figure 4 shows a fluorescence micrograph of such a mixture with 19 mol% of the mesogen incorporated ($T = 20 \pm 1\,^{\circ}\mathrm{C}$, $\pi = 14$ mN/m, $A = 62$ Å^2). The snapshot shows a number of dark domains, qualitatively similar to one another except for the fact that $n = 1$, 2, 3, or 4 spiral arms are grown from the respective nucleation centers. One-armed domains—such as the one indicated by an arrow—have the appearance of mirror symmetry; however, closer inspection reveals that one of their ends—the one from which growth was nucleated—is filled, whereas the other one is empty (see also magnified views in Fig. 7, below). Between these two ends, the body of the domains curve left-handedly in a delicate (thickness, ≈ 1 μm) spiral that opens—due to repulsion from the nucleation center—and then closes again to form the terminus. The contour length of such a domain may be up to 20 μm. As with enantiomeric DPPC, all such domains show the same direction of the curvature, regardless of how many arms emerge from its center. For our purpose it is irrelevant whether the mesoscopic chirality emerges from the molecular property of the DPPC or the 5CB: The system just serves as a case to test whether structure formation may be quantitatively modeled using the concept of spontaneous curvature—inferred from molecular chirality—as developed in Sec. III B.

B. Effective pair potentials and spontaneous curvature

To develop a reasonable contribution to the Hamiltonian of the system that accounts quantitatively for molecular chirality, we start by evaluating the effective pair potentials (EPP's) [41] between two adjacent amphiphilic molecules within the monolayer film. Figure 5 shows a top view of two such molecules, modeled as soft bodies with two chains each (for simplicity, their orientation is taken to be normal to the surface). An angular offset between the pseudomirror symmetry plane bisecting the chains and the horizontal direction from the β chain to the headgroup results from the molecule's chirality. Due to the vectorial orientation of the lipids within the film, the headgroups of both molecules are located

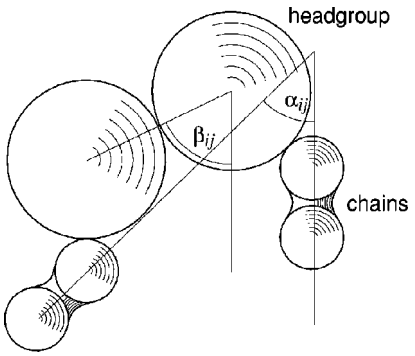

FIG. 5. Molecular arrangement in the EPP mapping: top view of two lipid molecules in the monolayer plane, and definition of the coordinates used to describe their mutual orientation. The distance between the headgroups was fixed in the mapping.

at the same height, underneath that of the chains. If one fixes the distance between the headgroups, and keeps the intramolecular coordinates constant, only two angular coordinates are left, describing the relative orientation of the two lipids within the film: α_{ij} accounts for the relative orientation of the backbones within the plane of the film, and β_{ij} characterizes the direction connecting the two headgroups with respect to a reference axis, cf. Fig. 5.

The interaction potential of the two soft bodies, ϕ, incorporates two major contributions: the van der Waals attraction ϕ_{vdW}, and a soft penetration repulsion ϕ_{rep} which we take to be proportional to the penetrated volume if the two bodies are located closer in space than their static van der Waals radii would permit. Thus two cylindrical soft bodies with static van der Waals radii r_1 and r_2 experience the interaction potential

$$\phi(r) = \begin{cases} \phi_{vdW}(r), & r > r_1 + r_2 \\ \phi_{rep}(r), & r \leq r_1 + r_2, \end{cases} \tag{1}$$

with

$$\phi_{rep}(r) = \theta_{soft} V_{penetr} = \theta_{soft} A_{penetr} \Delta z, \tag{2}$$

where V is a volume, A is an area within the surface film, and z is the direction of the surface normal.

The mutual energy of the two molecules includes a steric repulsion term and several dipole-dipole interactions. The steric repulsion is accounted for by an energy deriving from a deformation of the virtual volume of the chains. The concept of a ''virtual volume'' is motivated by the fact that the time scales of molecular vibrations and linear molecular motions are quite different. As the virtual volumes of two molecules overlap, the free volume associated with those molecules shrinks, and their degree of freedom is reduced: The energy of the system rises. Dipole-dipole interaction is a superposition of contributions from moments parallel to the surface interacting with each other and moments perpendicular to the surface interacting with each other. From a molecular point of view, normal components contribute only weakly to the molecular interactions because of their image dipoles and intramolecular compensation of parallel and antiparallel moments. Their interactions, however, are not negligible for the entire domain, since they do not average to zero over the domain area. In contrast, dipoles parallel to the surface are

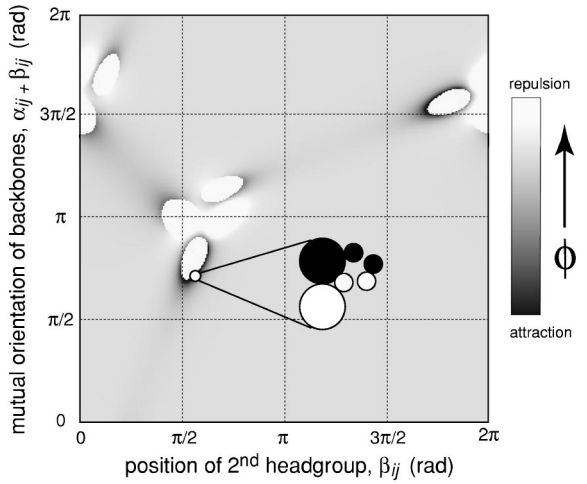

FIG. 6. Effective pair potential map of the molecular arrangement shown in Fig. 5. The repulsive interaction has been truncated in the plot. For details, see the text.

enhanced by their image dipoles; as they form higher multipoles with neighboring molecules, on the other hand, they are of short range and do not contribute to the domain energy. However, these in-plane dipoles contribute the major part to the *inter*molecular interactions. For a discussion of the relative contributions of lipid headgroups and chains, see Sec. III C.

The resulting EPP map ϕ vs α_{ij} and $(\alpha_{ij}+\beta_{ij})$, of the two molecules shown in Fig. 5, is displayed in Fig. 6. The gray scale representation has been optimized to emphasize the (shallow) minima (dark grays), which border regions of strong repulsion whose maximum values lie far beyond the brightest level, truncated at white. Most regions are just a uniform medium gray, corresponding to a faint attractive potential quite close to neutral. While the precise surface topology of the map is insignificant because details of the underlying molecular model were somewhat arbitrarily chosen, one recognizes two important qualitative features.

(a) Most importantly, the EPP map is not characterized by a simple symmetry. There are two rather confined regions—related with the two molecules in the system—in which both net repulsion and net attraction occur close to each other, forming a characteristic pattern within the map. One of these patterns, centered at $(\alpha_{ij},(\alpha_{ij}+\beta_{ij})) \approx (\pi, 0.6\pi)$, is the mirror image of the other pattern, centered at $(\alpha_{ij},(\alpha_{ij}+\beta_{ij})) \approx (1.6\pi, 0)$.

(b) There is a well-defined coordinate $(\alpha_{ij,0}, \beta_{ij,0})$, in which the mutual attraction finds its maximum. Generally, potential minima are observed located in confined regions within the (α_{ij},β_{ij}) plane. The most pronounced of those attraction zones borders one of the four unique repulsion regions in a narrow ditch; other attraction zones, albeit more shallow, are somewhat distributed between the repulsion zones.

C. Free energy of domain shapes

As a result of the observations made in the previous two sections, we write the free energy that determines the shape of a domain of chiral lipid molecules within a monolayer surface film as

$$E = E_{line} + E_{elstat} + E_{chiral}. \tag{3}$$

The first two contributions to the total free energy, the interfacial energy E_{line} and the electrostatic energy E_{elstat}, were extensively discussed in the literature [2,24]. They are given by

$$E_{line} = \lambda \oint_{\delta D} ds \tag{4}$$

and[4]

$$E_{elstat} = \frac{\mu^2}{2} \int_D \int_D \frac{dA\, dA'}{|\vec{r}-\vec{r}'|^3}, \tag{5}$$

in which λ denotes line tension, μ denotes the dipole moment difference per unit area between the condensed domain and its disordered surrounding, and D and δD are the area and the perimeter of the domain, respectively. Due to their location within media of different dielectric constants (ϵ_r), separated by the hydrophilic-hydrophobic interface, group dipole moments on lipid chains and headgroups behave entirely different with respect to long-range accumulation of their interactions. Both headgroup and chain dipoles give rise to image charges located across the interface: Terminal methyl groups and carbonyls on the chains are embedded in a medium of $\epsilon_r \approx 2$; the normal components of their image dipoles have the same directions as those of the real dipole moments. As a consequence, their effective dipole moments, deriving from the superposition of real and image dipoles, are *normal* to the interface—giving rise to long-range repulsion. In contrast, headgroup dipole moments are located in an environment with $\epsilon_r \gg 10$, and give rise to image dipoles whose projections on the surface normal have the *opposite* directions to that of the real dipoles. Although headgroup dipole moments are generally much larger than those of the chains, their normal projections are thus canceled by those of their image dipoles; the resulting superposition has an in-plane orientation, and leads to quadrupolar charge distributions of only short-range interaction.

To formulate a contribution of the molecular chirality to the total free energy, we utilize the properties of the derived EPP map, namely, its asymmetry and the fact that it contains (at least) one pronounced minimum. Taking into account that one of the coordinates is arbitrarily chosen, one finds one specific angle corresponding to the energy minimum. Placing the molecule into a (pseudo) unit cell introduces two intermolecular distances Δ_1 and Δ_2. A similar pseudo-unit-cell containing a neighboring molecule is necessarily misaligned with respect to the first one: Any attempt on a realignment leads to an increase in energy. Only if the EPP map is symmetric may a unit cell be found that extends over two (or more) molecules and sustains the formation of a true crystal lattice. The angle of misalignment in connection with Δ_1 and Δ_2 yields two spontaneous curvatures, $k_{1,0}$ and $k_{2,0}$.

[4]Since we will solve the energy minimization numerically on a mesoscopic grid (*vide infra*), we need not be concerned with the singularity that arises as $\vec{r} \to \vec{r}'$.

The Taylor expansion of the potential around its minimum leads to a quadratic approximation described by the Hesse matrix **H**. Thus the contribution to the free energy due to the shape of the molecules may be written as

$$E_{chiral} = \int_D (k_{1,0}-k_1, k_{2,0}-k_2)^T \mathbf{H} (k_{1,0}-k_1, k_{2,0}-k_2)\, dA$$
$$= \Delta \vec{k}^T \mathbf{H} \vec{k}\; dA. \tag{6}$$

1. Quasi-1D, curved domains

Assume a pronouncedly elongated, curved domain for which all contributions to E across its (small) dimension perpendicular to the growth direction are essentially zero. In such a case, the dimensions of the integral expressions [Eqs. (4), (5), and (6)], are all reduced by one unit. The contribution due to line tension simplifies to $E_{line} = 2\lambda l$ (where l denotes the total length of the elongated domain); this is obviously a constant with respect to the domain shape γ, which need not be explicitly included in the calculations. The electrostatic energy reduces to

$$E_{elstat} = \frac{\mu^2}{2} \int_\gamma \int \frac{ds\, ds'}{\gamma |\vec{r} - \vec{r}'|^3}, \tag{7}$$

while only one spontaneous curvature is required to determine the chiral contribution

$$E_{chiral} = \xi \int_\gamma (k(\vec{r}) - k_0)^2\; ds, \tag{8}$$

in which $\xi = H_{11}$ is a scale factor and is the actual curvature of the domain at $\vec{r}(s)$. The curvature may be evaluated as

$$k(\vec{r}) = \frac{|\dot{\vec{r}} \times \ddot{\vec{r}}|}{|\dot{\vec{r}}|^3}. \tag{9}$$

The solution of $\delta E_{total} = 0$ leads to an integrodifferential equation, which cannot be solved analytically or using Runge-Kutta's algorithm. We have thus chosen to determine γ, the domain shape, by using an iterative approach to minimizing the contour energy. The domain is composed of successively larger numbers of straight segments, characterized by equidistant kink points, that approximate the macroscopically curved contour line. Each kink point is specified by a triple of coordinates: two local Cartesian coordinates and an angle α that characterizes the kink. α is related to the local curvature by

$$k = \frac{1}{R_\alpha} = \frac{\sin \alpha}{2\Delta \sqrt{2 - 2\cos \alpha}}, \tag{10}$$

where R_α is the radius associated with the curvature of the domains, and Δ is the length of the segment. More specifically, R_α is the outer radius of the triangle defined by two neighboring segments. In practical terms, two free parameters determine the 1D shape of the domains,

$$\zeta = \frac{\mu^2}{2\xi}, \tag{11}$$

a reduced dipole moment density (normalized to the chiral contribution in a similar way as in the normalization to the line tension in earlier assessment of 2D domain shapes without a chiral energy contribution [25]), and the spontaneous curvature k_0 normalized to the length of the domain. In distinction from earlier work, no dependence of λ on the location of a line segment at the perimeter of the domain has been assumed.

The evaluation starts with $n = 3$ segments, with values corresponding to the spontaneous curvature, and minimizes their total energy by adjusting α at each kink point. This may be achieved by a straightforward steepest decent algorithm, since only one degree of freedom is involved in the minimization problem. In the iteration of this process, the number n of kink points along the contour line is successively increased by one until a preset value is reached. This algorithm works well with any number N of spiral arms emerging from a domain nucleus. If $N > 1$ arms are involved in the energy minimization, electrostatic interaction is taken into account within each of the arms as well as between them.

In Fig. 7, results from the energy minimization are compared with experimental observations. Figure 7(a) shows a largely magnified image of a one-armed domain taken from an image similar to Fig. 4. The domain's nucleus is located in the lower left section of the image, and growth occurs from there in an opening and subsequently narrowing spiral to the termination point in the upper central section of the image. The result of an energy minimization ($n = 100, \zeta = 8, k_0 = 0.12$) is overlaid to the experimental image, and the agreement between both contours shows clearly that the approach which we have developed is quite adequate to assess the morphology of the quasi–1D domain. Likewise, in Fig. 7(b) the modeling of a two-armed domain is compared with an experimental result. Not surprisingly, these parameters are identical to those that have been found in modeling the situation shown in Fig. 7(a). One realizes that the domain shape close to the nucleation point in the center of the image is quite different from its shape near the termination points of the two spirals. This feature, as well as the overall shape of the domain, is faithfully reproduced in the model. In conclusion, from the comparison of the model with the experimental results contained in images such as Fig. 4, it is recognized that the concept of spontaneous domain curvature is quite well suited to describe the contour shapes of elongated domains with narrow cross sections.

2. 2D domains

The concept of a 2D spontaneous curvature for the description of domain shapes of chiral lipids in surface monolayers leads to general problems. To our knowledge, there is no general mathematical theory that uniquely identifies the curvature in two dimensions of an area of arbitrary, continuous shape. For the evaluation of experimental results in the form of an assessment of the curvature of the local directors describing the collective tilt of aliphatic chains in a monolayer, we made the following assumptions.

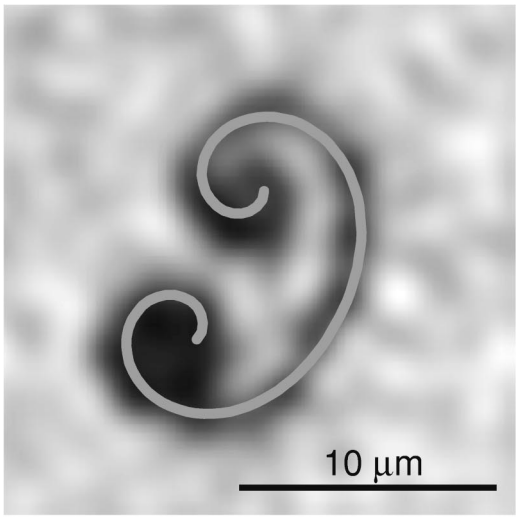

(a)

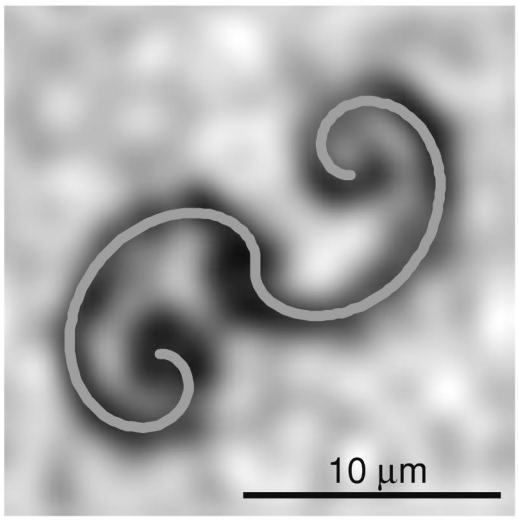

(b)

FIG. 7. Comparison of 1D models with experimental data similar to those shown in Fig. 4. (a) One-lobed domain. (b) Two-lobed domain.

(1) Each single connected region D can be obtained from the unit square E through a coordinate transformation. As this mapping is at least single valued, there is a function $f: E \mapsto D$.

(2) E may be parametrized using Cartesian coordinates. This parametrization yields two curvature values at each point within D which are associated with orthogonal directions within E:

$$\vec{k}(\vec{r}) = (k_x(\vec{r}), k_y(\vec{r})),$$

$$k_x(\vec{r}) = k_x(x,y) = k_x(x)|_y, \tag{12}$$

$$k_y(\vec{r}) = k_y(x,y) = k_y(y)|_x.$$

To minimize the energy, a Monte Carlo method has been implemented that determines the vector $\vec{k}$ used to transform the coordinates of the unit square E into the target shape D. This procedure facilitates domain energy minimization that includes the chiral contribution, according to Eq. (6), by adjusting the mapping f. In the evaluation, the dual area integration in Eq. (5) has been evaluated by simplifying the expression using Green's theorem [25]:

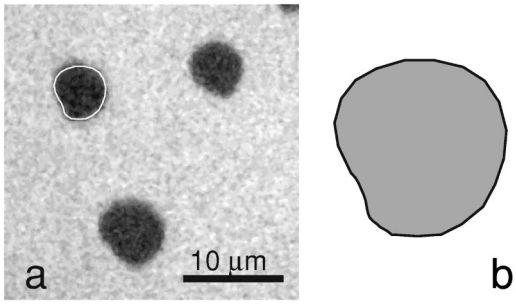

FIG. 8. Comparison of a 2D model (b) with experimental data (a): L-DPPC on water shortly after the onset of the phase transition.

$$\int_D \int_D \frac{dA\, dA'}{|\vec{r}-\vec{r}'|^3} = -\oint_\gamma \oint_\gamma \frac{ds\, ds'}{|\vec{r}-\vec{r}'|}. \tag{13}$$

The Monte Carlo procedure acts on a unit square E characterized by $n \times m$ grid points. We found that this algorithm is susceptible to instabilities with respect to the crossover of gridlines in the target shape D when going to small line tension values. In order to obtain a good appreciation of the internal structure of D, it is obviously necessary to construct a well-distributed grid within the target shape. Thus a penalty function was introduced which favors grid points at even distances. The contribution of this penalty function to the final results was kept below 10% of each of the remaining (physical) terms.

As to a comparison with experimental results, we were limited to the analysis of situations in which domains are well separated from each other, because the algorithm performed poorly with respect to instabilities (gridline cross over) if electrostatic interdomain interactions are taken into account. Moreover, the algorithm is too inefficient to enable an extensive modeling of the 2D situation on the workstation we used for the computations. This implies that only situations could be analyzed in which the domains have just been nucleated and growth has not proceeded much further, limiting us to a comparison of models with small domains that have not yet grown into their mature, characteristic forms. Nevertheless, a quantitative comparison is feasible: Figure 8(a) shows three juvenile domains in a monolayer of pure L-α-$DPPC$ on water ($\pi = 8$ mN/m, and $A = 72$ Å^2) of a similar preparation that leads to morphologies such as those shown in Figs. 1 and 2 upon further compression of the surface film. Although the diameter of the domains is only ≈ 10 times the optical resolution, it is appreciated that the domains are not circular but rather kidney shaped, and not even mirror symmetric. All three domains show the same deviation from mirror symmetry, which is obviously associated with the chirality of the system—although it is not obvious at that stage of domain growth how the handedness of the domain shapes relates to the molecular chirality. A representative model of a domain shape with minimal energy [$2\lambda/\mu^2 = 30$, $H_{11} = 30$, $H_{22} = 10$, $H_{12} = H_{21} = 15$, and $\vec{k} = (1,5)$] is presented in Fig. 8(b), and overlaid with one of

the experimentally observed specimens. As in a comparison of energy-minimized shapes with quasi-1D domains, it is obvious that the model is quite capable of capturing the essential features of the structure formation in two dimensions in the experimental system.

3. Crowded domains in a quasi 1D approximation

The most complex form of structure formation in lipid monolayers is one in which domains have come so close to one another upon growth that electrostatic interdomain interactions become substantial. In a number of experimental studies, situations were reported in which this occurs at relatively small values of λ, such that the resulting domains are elongated, forming effectively a 1D lamellar phase (stripe phase) [23,24]. In a few cases, a continuous development of such stripe phases upon film compression or temperature variations was reported [12,29].

Textures that occur in such situations, e.g., in monolayers of DPPC or DMPA mixtures with cholesterol, are distinguished from the results observed in the DPPC/5CB system, (Fig. 4) in the following respects.

(i) The area fraction of the ordered phase is much larger in the mature DPPC/cholesterol system than in DPPC/5CB.

(ii) Growth in the crowded situation leads to interdigitation of arms from different domains.

(iii) Depending on the system and the experimental conditions, growth in the crowded situation may lead to branching of the domains. Such branching has been extensively studied by various groups [17,18,27].

In order to assess this situation in model calculations, the technique based on Eqs. (7) and (8) needs to be only marginally extended: Equation (7) is modified to include both intradomain and interdomain electrostatic interactions:

$$E_{elstat}=\sum_{i,j}\frac{\mu^2}{2}\int_{\gamma_i}\int_{\gamma_j}\frac{ds\,ds'}{|\vec{r}-\vec{r}'|^3}. \tag{14}$$

The contribution for $i\neq j$ has to be included as the mean distance $\langle d\rangle$ between domains becomes comparable with their mean diameter. For model calculations, either periodic boundary conditions or the simulation of domain growth in a 2D potential well lend themselves for the implementation. We have chosen the latter option, and simulated domains shapes in an external potential with soft walls, compromising on the susceptibility of this method for edge effects for its relative ease of implementation due to its confinement to finite summations. As an analytic form of the external potential at the walls we chose a parabolic function to confine the domains to the center of a square potential well. Within the well, the potential energy of a domain segment is equal to zero.

The calculation of the model shape follows the pattern spelled out for the assessment of isolated quasi-1D domains: A number of domain nuclei is distributed at random within the potential well. The number of segments is incremented, and the local kink angle α at the joints of the segments adjusted to minimize the total energy of the arrangement of domains until a preset length of the domains, corresponding to a particular area fraction of the ordered monolayer phase, has been reached. As a deficiency of the implementation, the algorithm is susceptible to the crossover of the quasi-1D domains, particularly at the well boundaries. In addition, highly curved structures may occur close to these boundaries, depending on the arbitrarily chosen starting conditions. Consequently, a comparison of the models with experimental results is limited to the central sections of the well.

Another significant complication in the comparison of modeling results with experimental observations arises in that both types of results depend largely on the starting condition, i.e., the locations of the randomly occurring or randomly chosen domain nucleation sites in the experimental situation or the Monte Carlo model, respectively. Yet both classes of starting conditions sensitively determine the detailed arrangements of the domain ensembles. Since these starting conditions never coincide, a direct comparison—similar to the one afforded in the previous sections—is not feasible. Instead, one has to compare the similarity classes of domain ensembles in experiments and in model calculations in order to quantify the correspondence between a computed morphology and a given experimental result. We have applied integral geometric methods [42] to afford a quantitative comparison of the morphology patterns formed by domain ensembles.

4. Minkowski measures

A coordinate in Minkowski space which characterizes the content of an image containing an arbitrary irregular pattern is defined by a triplet of functions, s, ν, and χ. The argument of these functions depends on the character of the images that are to be compared. For the general case in which images with a full dynamic gray range are of interest, the analysis starts by slicing the image at any available gray level ρ. In such a case, ρ represents the argument of the Minkowski functions, which are the normalized portion of black pixels, $s(\rho)$; the normalized length of the border between black and white regions, $\nu(\rho)$; and the normalized *Euler* function, $\chi(\rho)$, i.e., the difference of the number of the connected black and white regions. In concert, these functions define the pattern quite sensitively, and depend very weakly on the chosen part of the image. Scaling the image by a factor n leads to the following rescaling laws for the Minkowski functions: $s_1=s_2$, $\nu_1=\nu_2/n$, and $\chi_1=\chi_2/n^2$.

To access these functions for an image that contains essentially two gray scale levels—such as the ones analyzed here—, the image is sliced while the threshold is placed at the minimum of the bimodal gray level distribution. Since we are concerned with elongated domains, the width of these domains is of minor importance for the assessment of the underlying pattern. Consequently, we have skeletonized the images in the next step of the analysis using the built-in function of the NIH Image package. The resulting pattern of curves—one pixel wide—is well suited for a quantitative comparison with the computed patterns. Since the Minkowski functions require 2D regions within the images to be compared, one has to transform the stripe patterns back into 2D connected regions in a controlled manner. On each black pixel we have placed a circle with radius ρ ($\rho=1,2,\ldots$), which represents the argument of the Minkowski functions in the application of the formalism as described here. For more details and an example of the trans-

formations applied to an experimental image, cf. the Appendix.[5]

To quantify the similarity of two images, their distance in Minkowski space has to be determined. This distance is defined as

$$a=\int_0^\infty (s_1(\rho)-s_2(\rho))^2\,d\rho+\int_0^\infty (\nu_1(\rho)-\nu_2(\rho))^2\,d\rho + \int_0^\infty (\chi_1(\rho)-\chi_2(\rho))^2\,d\rho. \tag{15}$$

We observed that all three Minkowski functions converge uniformly to zero as the shapes of patterns converge toward each other, and have thus confined the quantification to analysis of only $\chi(\rho)$. Since the scaling between simulated and experimental images is *a priori* unknown, we have calculated a as a function of the scaling factor n of the simulated images. Two images were then accepted to be similar if their distance in Minkowski space at any n falls below the square of the modulus a_0 of the unscaled experimental image:

$$a_\chi=\int_0^\infty (\chi_{expt}(\rho)-\chi_{mod}(\rho))^2\,d\rho \leqslant 0.1\int_0^\infty \chi_{expt}^2(\rho)d\rho. \tag{16}$$

5. Ensemble domain shapes

Figure 9 shows two examples of experimental data for DMPA plus 4 mol % cholesterol on an aqueous solution of 5 mM NaCl and 10 μM EDTA, adjusted to pH=11 with NaOH. Figure 9(a) has been taken at $T=10\,^\circ$C and $\pi \approx 14$ mN/m, and Fig. 9(c) at $T=4\,^\circ$C and $\pi \approx 8$ mN/m. The experimental images are compared to energy minimized ensemble arrangements that were computed using the following input parameters. The thickness of the bodies of the computed domains is chosen to obtain a reasonable correspondence to the observed experimental shapes. It has to be emphasized that the synthetic ensemble textures shown are not necessarily the best possible matches: Due to limited computing power, we have not systematically screened parameter space on a close-meshed grid; moreover, even under identical parameters different explicit textures will be found depending on the starting conditions. However, visual inspection already shows that the correspondence between the two pairs of patterns is striking: In the data set at $T=10\,^\circ$C, the relatively short domain bodies are organized on pseudogrid lines that form a striped pattern which extends from the top of the micrograph to the bottom. This feature is faithfully reproduced in the synthetic pattern [Fig. 9(b)]. Moreover, as indicated by the two dashed lines overlaid on both the experimental and simulated data, the sequence of neighboring domain shapes *may* develop very similar in both cases. Clearly, the close correspondence in the depicted example is fortuitous—under slightly different starting conditions, it could have occurred in a significantly different manner, or it could have been found in a mirror-symmetric arrangement. However, its occurrence suggests strongly that the images compared in Figs. 9(a) and 9(b) are certainly *similar* to each other. On a more quantitative basis, we note that the distance of the Euler functions χ of the two images is much smaller than the square of the modulus of the experimental image: $a_\chi \approx 0.088 a_{\chi,0}$.

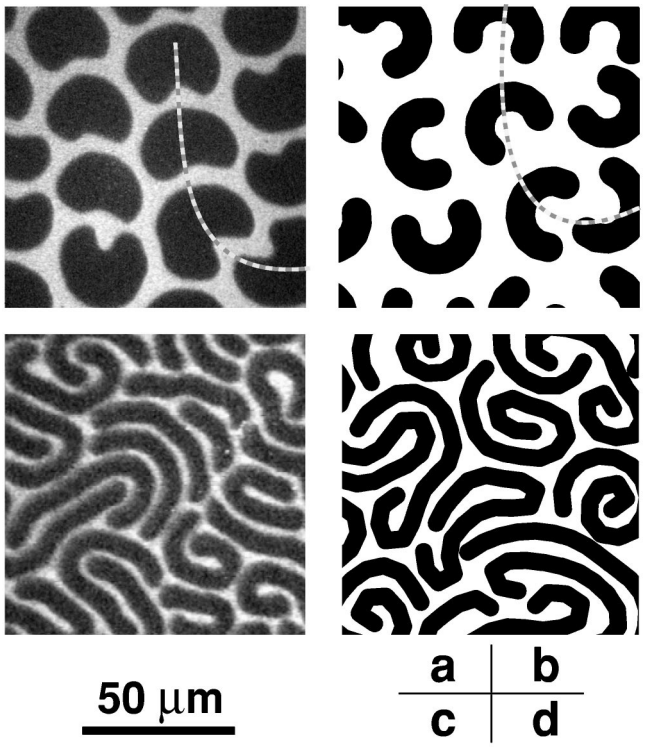

FIG. 9. Comparison of 1D models (b) and (d) with experimental data [(a) and (c): L-DMPA with 4 mol % cholesterol on an aqueous subphase at pH=11 and 5 mM Na^+, 10 μM EDTA] at $T \approx 10\,^\circ$C, $\pi \approx 14$ mN/m (a) and $T \approx 4\,^\circ$C, $\pi \approx 8$mN/m (b). The Minkowski distances between the simulated and the experimentally observed data are $a_\chi \approx 0.088 a_{\chi,0}$ [(a) and (c)] and $a_\chi \approx 0.090 a_{\chi,0}$ [(b) and (d)]. The dashed lines in (a) and (b) indicate a succession of domains that happened to develop quite similarly in the experiment and the simulation—beyond the general similarity of the underlying patterns.

At a lower temperature, $T=4\,^\circ$C [Figs. 9(c) and 9(d)], the textures in the monolayer have generally elongated, transforming the phase morphology into a striped pattern. The pseudorows observed in Fig. 9(a) disappear and neighboring domain bodies interdigitate deeply alongside each other. However, the correlation length of the striped pattern is extremely short as the texture incorporates a large number of defect points. Again, these features are faithfully resembled in the simulated image [Fig. 9(d)], which shows hairpin shapes formed by individual domains as well as elongated forms that are squeezed in between more compact domains. Quantitatively, the Euler functions of the two images are close to each other, $a_\chi \approx 0.09 a_{\chi,0}$ [for comparison, the Minkowski distance between the Figs. 9(b) and 9(d) is $a_\chi \approx 50 a_{\chi,0}$].

IV. DISCUSSION

The experimental results presented in Sec. III as well as previous work clearly show that the chirality of lipid mol-

[5]This technique is known as ''erosion/dilation operation'' in the mathematical literature [60].

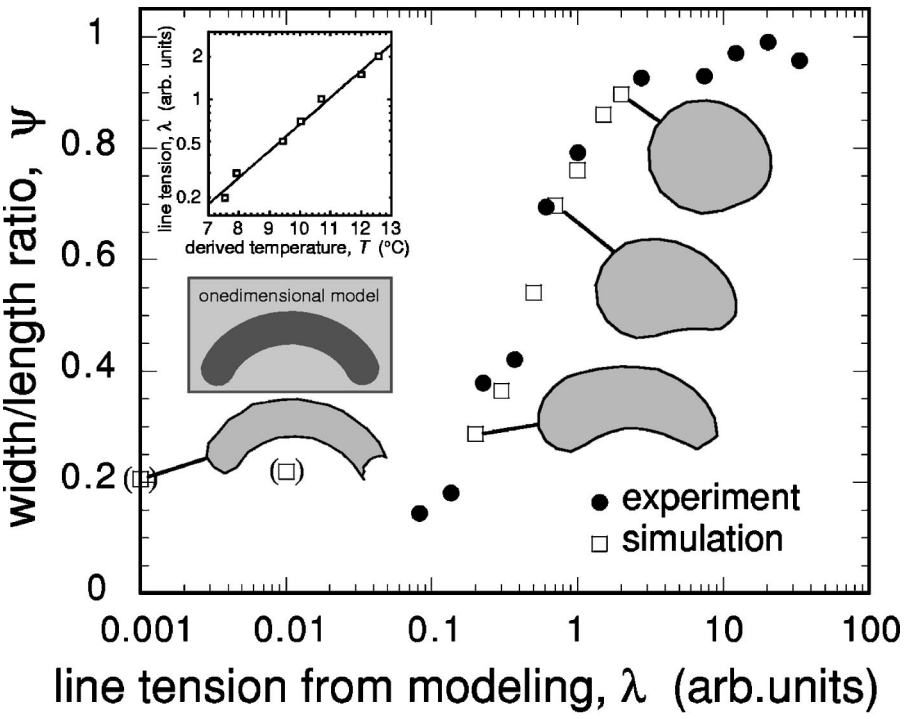

FIG. 10. Correlation, via the width-length ratio ψ of the domains, of the temperature dependent shape transformations observed for L-DMPA/4 mol % cholesterol with 2D simulations in which only the line tension λ was adjusted and all other parameters were kept constant. Some of the experimental data were shown in Fig. 9. The experimental data were collected between $T=17\,^{\circ}\mathrm{C}$ (highest λ) and $T=3\,^{\circ}\mathrm{C}$ (lowest λ). The inset graph shows the correlation between T from the experiment and λ from the simulations. The sketches on the left hand side demonstrate that the 1D and 2D simulations at low ψ yield the same results. The simulation results shown in parentheses at low λ are believed to lie systematically too high in ψ due to problems with the algorithm.

ecules affects pattern formation in aqueous surface monolayers sensitively. We have derived a formalism that accounts quantitatively for the contribution of chirality to the energy of the system, and have shown that one may model experimentally observed textures by accounting for line tension, electrostatic interactions, *and* chirality in a wide range of experimental situations. With this development, we have paved the road to simulating domain morphologies in surface monolayers in their full complexity, i.e., for complex 2D shapes in a crowded situation where domain-domain interactions are substantial—such as the one shown in Fig. 2.

What can be learned from such simulations in terms of the molecular properties of the system? Clearly, the observed mesoscopic structures reflect details of the molecular interactions which might be quantified upon systematically studying the molecular parameters used to model the experimental results. Unfortunately, since the computation of equilibrium shapes derive from a continuum theory, the absolute length scale has been lost and the molecular parameters may only be determined in relation to one another. While the absolute magnitudes may be determined using thermodynamic relations [43] or micromanipulation [44,45], it is also interesting to assess the trends that the system follows upon continuous variation of thermodynamic parameters. As shown in earlier work [29], the DMPA/cholesterol system at high pH undergoes a continuous transition from a pseudohexagonal phase to a striped phase upon lowering the temperature T at a fixed area A. While the original data[6] are too poor in quality for an analysis as outlined Sec. III, we have repeated such a measurement for a quantitative evaluation. Consistent with the earlier work we find an elongation of the domains—indicative of a reduction of the line tension λ— upon falling T. Two representative images from this measurement are shown in Figs. 9(a) and 9(c). Figure 10 visualizes a correlation of the experimental results with simulated data. In both cases, the width-length ratio ψ has been determined as a quantitative measure of domain elongation, and ψ has been plotted as a function of λ for the simulation results (in arbitrary units, since the modeling of the domain shapes yields only the ratio $2\lambda/\mu^2$). The relation $\psi=\psi(\lambda)$ is clearly sigmoidal, showing a large drop in ψ upon lowering λ within a narrow regime, while ψ stays essentially constant above and below this transition regime. In a second step, ψ has been determined as a function of T for the experimental data. Finally, by using the implicit interdependence, λ has been mapped to T. From this mapping we derive an exponential relation $\lambda=\lambda_0 e^{aT}$ (see the inset in Fig. 10). In the main body of the figure, this linear mapping has been utilized to compare the simulation results with the rescaled experimental observations, and it is revealed that the correspondence between the two is almost perfect. At low λ, the models suggest ψ ratios that are systematically large. This is attributed to inherent difficulties of the simulation algorithm. For reference, some of the simulated domain shapes are included in

[6]We thank Dr. W. Heckl, Munich, for providing the original data contained in Fig. 3 of Ref. [29].

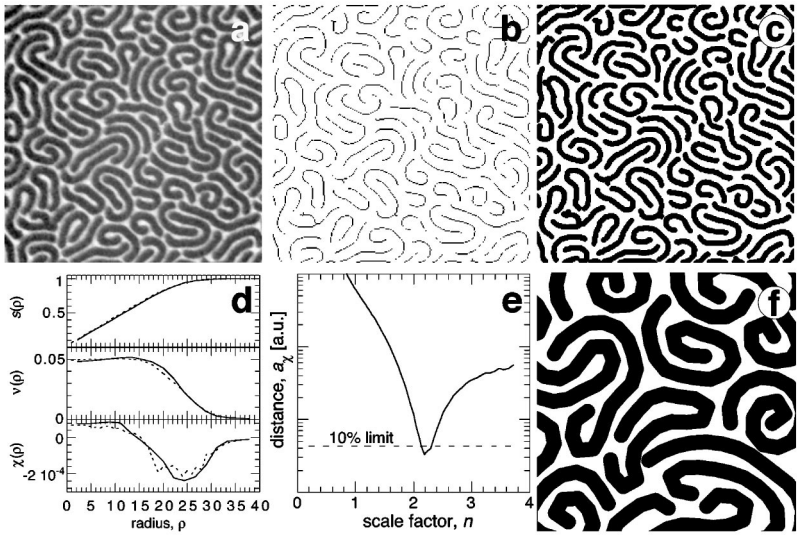

FIG. 11. Image processing and the quantification of Minkowski distances between experimental and simulated data. (a) Background corrected raw data. (b) Raw data sliced and skeletonized. (c) Skeletonized data after adjustment of domain thickness to radius ρ. (f) Simulated unscaled data with adjusted domain thickness. (d) Comparison of the Minkowski measures s, ν, and χ. (e) Distance a_χ between the experimental and simulated data as a function of the scaling factor n.

Fig. 10 and related to the corresponding data points. As indicated on the left hand side of the main panel, the domain shape emerging from the 2D modeling with vanishing λ is identical to that emerging from the 1D models if one fixes the latter with the appropriate domain width.

It is important to note that elongation depends critically on the molecular chirality under equilibrium conditions: Elongated structures are generally not observed in monolayers of achiral amphiphiles—such as fatty acids or esters—and, on the other hand, we have not observed a transition such as the one shown in Fig. 10 in simulations in which $\mathbf{H}=\mathbf{0}$ has been assumed. While transitions from circular to noncircular domains have been found in systems that are exclusively determined by line tension and electrostatic repulsion [31], we note that in practical terms such systems are kinetically trapped in the circular state such that an actual transition is *only* observed if chirality is added as an ingredient in the Hamiltonian of the system.

The symmetry break in the molecular arrangement within phospholipid domains due to the molecules' chirality leads to a consequence that may be experimentally tested. If one compares coherence lengths of the hexatic lattices formed by the alkyl chains of different compounds, achiral molecules should have longer correlation than chiral ones. Fortunately, such coherence lengths may be experimentally determined in GIXD experiments [34,46,47]. Unfortunately, 2D lattices in general are subject to low energy lattice distortions, prohibiting the formation of crystals with infinite correlation lengths [48,49]. We estimate the contribution of chirality to reducing the correlation length of the positional order of scattering centers in Langmuir monolayers as follows.

The spontaneous curvature k—as revealed from the modeling in correspondence with the experimental data—determines the displacement b of a molecule, located at a distance $D=n\Delta$ (Δ is a lattice constant) from the origin, from its proper lattice site. As b becomes comparable to Δ upon increasing the number of lattice spacings n, positional correlation is lost due to the molecular chirality in an otherwise ideal system. With

$$b=\frac{1-\cos nk\Delta}{k}\approx\frac{n^2k\Delta^2}{2} \tag{17}$$

and $D\approx 5$ Å and $k\approx 1\ \mu\mathrm{m}^{-1}$, we arrive at $n\Delta\approx 320$ Å for the correlation length. We propose that molecular chirality reduces the correlation length in addition to the limitations imposed due to the dimensionality of the system, and estimate from our results for the spontaneous curvature that $n\approx 60$ lattice constants should pose an upper limit for L-DPPC. There have in fact been a number of GIXD studies of phospholipid monolayers in the literature (for a recent review, see Ref. [50]). While PA's [51,52] and PE's [53,54] were the objects of numerous studies, and were reported to yield diffraction peaks that are close to instrumentation limited ($n\Delta\approx 1{,}000$ Å), there is to, our knowledge, only one study published that shows rather broad diffraction peaks from (enantiomeric and racemic mixtures of) DPPC [55]. Whereas all phospholipids are chiral, the impact of chirality on the microscopic and mesoscopic structure is determined by the headgroup size in relation to the cross section of the aliphatic chains: PA's and PE's—which are characterized by small headgroup sizes—develop by and large circular domain morphologies [51,56–58], while DPPC with its bulky headgroups shows a pronounced fingerprint of molecular chirality both in the mesoscopic domain shape and a low correlation length. Along this line of argument, *triple*-chain PC,[7] for which the ratio of the headgroup size and the aliphatic chain cross section is again reduced, shows both circular domain morphologies in FM and extended correlation lengths in GIXD (see Figs. 3 and 5 of Ref. [59], respectively). It might be worthwhile to study the interrelation between the impact of molecular chirality on domain textures and correlation lengths in GIXD more systematically in the future.

V. CONCLUSIONS

We have shown that the molecular chirality of phospholipids sensitively determines the morphology of liquid-condensed domains in aqueous surface monolayers, and have developed a concept for the calculation of such morpholo-

[7] 1-hexadecyl-2-(2-myristoyl-palmitoyl)-3-glycero-PC and 1-(2-myristoyl-palmitoyl)-2-hexadecyl-3-glycero-PC [59].

gies which is directly related to the molecular asymmetry. The contribution of chirality to the Hamiltonian of the system is sizable for species such as DPPC for which the chirality is paired with a large size of the headgroup in relation to the cross section of the aliphatic chains; this leads to a spontaneous curvature of the domains within the plane of the monolayer. With this concept, we have been able to simulate realistically the domain shapes in a number of experimental situations with progressively higher complexities under equilibrium conditions. In two-dimensional simulations of domain shapes we have observed that a reduction of the line tension λ—normalized to the electrostatic repulsion between collinear dipole moments on the molecules—is a necessary, but not sufficient, condition for the formation of a striped phase: Elongated domains under equilibrium conditions appear only if the film-forming molecules are chiral. This is consistent with experimental observation: To our knowledge, stripes of solid and liquid-condensed phases formed by achiral amphiphiles have not been reported in the literature. Finally, we have argued that the spontaneous curvature of chiral domains is a major source for the reduction of the correlation length of the molecular positions in a hexatic lattice. This prediction should be experimentally tested in future work.

ACKNOWLEDGMENTS

We thank Dr. C. Lautz for the BAM image and Dr. H. Schmiedel for a sample of 5CB. This work was supported by the DFG through the Sonderforschungsbereich (SFB) 294, TP F3, and the priority program ''Wetting and Structure Formation at Interfaces'' under Contract No. Lo352/7-1. We also thank the Fonds der Chemischen Industrie, Frankfurt, for support.

APPENDIX

Figure 11 gives a rundown of the manipulations applied to experimental data for the quantification through the Minkowski measures as used to assess the similarity of growth patterns with simulated data. We start with a gray-scale image (upper row, left) which consists essentially of two gray levels. The raw data have been corrected for a slightly inhomogeneous illumination within the plane of the image. The gray-scale image is sliced and then skeletonized to yield connected trains of the domain's center lines that are just one pixel wide (upper row, center). Finally, black disks with radii ρ are placed on each black pixel along the trace of the domain's skeletons to obtain the pattern shown in the upper right, which may now be compared with a synthetic pattern (lower right) in which the domain bodies have also been widened to the same radius ρ for comparison. For the displayed examples, the three Minkowski measures $s(\rho)$, $\nu(\rho)$, and $\chi(\rho)$ are given on the lower left, where measures for the synthetic pattern are shown as solid lines and those for the experimental pattern as dotted lines. To determine the Minkowski distance between the two images, the quadratic difference a_χ of the Euler functions $\chi(\rho)$ are calculated according to Eq. (16) in dependence on a scale factor n (lower row, center), and the two patterns are assumed to be similar if the minimum of a_χ with respect to n falls below a threshold (chosen to be 10% of the modulus of the experimental image).

[1] H. Möhwald, Annu. Rev. Phys. Chem. **41**, 441 (1990).
[2] H.M. McConnell, Annu. Rev. Phys. Chem. **42**, 171 (1991).
[3] C.M. Knobler and R.C. Desai, Annu. Rev. Phys. Chem. **43**, 207 (1992).
[4] M. Lösche, E. Sackmann, and H. Möhwald, Ber. Bunsenges. Phys. Chem. **87**, 848 (1983).
[5] R.M. Weis and H.M. McConnell, Nature (London) **310**, 47 (1984).
[6] S. Hénon and J. Meunier, Rev. Sci. Instrum. **62**, 936 (1991).
[7] M. Lösche and H. Möhwald, Rev. Sci. Instrum. **55**, 1968 (1984).
[8] A. Fischer, M. Lösche, H. Möhwald, and E. Sackmann, J. Phys. (France) Lett. **45**, 785 (1984).
[9] L.A. Bagatolli and E. Gratton, Biophys. J. **78**, 290 (2000).
[10] S.L. Keller, W.H. Pitcher III, W.H. Huestis, and H.M. McConnell, Phys. Rev. Lett. **81**, 5019 (1998).
[11] S.L. Keller and H.M. McConnell, Phys. Rev. Lett. **82**, 1602 (1999).
[12] W.M. Heckl, M. Lösche, D.A. Cadenhead, and H. Möhwald, Eur. Biophys. J. **14**, 11 (1986).
[13] K.J. Stine, J.Y.-J. Uang, and S.D. Dingsman, Langmuir **9**, 2112 (1993).
[14] D.P. Parazak, J.Y.-J. Uang, B. Terner, and K.J. Stine, Langmuir **10**, 3787 (1994).
[15] H.E. Gaub, V.T. Moy, and H.M. McConnell, J. Phys. Chem. **90**, 1721 (1986).
[16] H.M. McConnell, J. Phys. Chem. **94**, 4728 (1990).
[17] K.-Y.C. Lee and H.M. McConnell, J. Phys. Chem. **97**, 9532 (1993).
[18] M.A. Mayer and T.K. Vanderlick, J. Chem. Phys. **100**, 8399 (1994).
[19] A. Miller, W. Knoll, and H. Möhwald, Phys. Rev. Lett. **56**, 2633 (1986).
[20] J.S. Langer, Rev. Mod. Phys. **52**, 1 (1980).
[21] M. Lösche, thesis, TU München, 1986.
[22] K. Nag, C. Boland, N. Rich, and K.M.W. Keough, Biochim. Biophys. Acta **1068**, 157 (1991).
[23] R.M. Weis and H.M. McConnell, J. Phys. Chem. **89**, 4453 (1985).
[24] D.J. Keller, H.M. McConnell, and V.T. Moy, J. Phys. Chem. **90**, 2311 (1986).
[25] H.M. McConnell and V.T. Moy, J. Phys. Chem. **92**, 4520 (1988).
[26] H.M. McConnell and Y.B. Bazaliy, Proc. Natl. Acad. Sci. U.S.A. **92**, 8823 (1995).
[27] M.A. Mayer and T.K. Vanderlick, J. Chem. Phys. **103**, 9788 (1995).
[28] J.S. Langer, Phys. Scr. **T9**, 119 (1985).
[29] W.M. Heckl and H. Möhwald, Ber. Bunsenges. Phys. Chem. **90**, 1159 (1986).
[30] H.M. McConnell, D.J. Keller, and H.E. Gaub, J. Phys. Chem. **90**, 1717 (1986).

[31] D.J. Keller, J.P. Korb, and H.M. McConnell, J. Phys. Chem. **91**, 6417 (1987).
[32] R. de Koker, W. Jiang, and H.M. McConnell, J. Phys. Chem. **99**, 6251 (1995).
[33] M. Lösche and H. Möhwald, J. Colloid Interface Sci. **131**, 56 (1989).
[34] J. Als-Nielsen and H. Möhwald, in *Handbook on Synchrotron Radiation*, edited by S. Ebashi, M. Koch, and E. Rubinstein (Elsevier, Amsterdam, 1991), Vol. 4.
[35] P. Krüger, M. Schalke, Z. Wang, R.H. Notter, R.A. Dluhy, and M. Lösche, Biophys. J. **77**, 903 (1999).
[36] C. Lautz, T.M. Fischer, M. Weygand, M. Lösche, P.B. Howes, and K. Kjaer, J. Chem. Phys. **108**, 4640 (1998).
[37] URL: http://rsb.info.nih.gov/nih-image/
[38] ftp://ftp-icf.llnl.gov/pub/Yorick/
[39] D.A. Cadenhead, F. Mller-Landau, and B.M.J. Kellner, in *Ordering in Two Dimensions*, edited by S.K. Sinha (Elsevier, Amsterdam, 1980).
[40] D. Vaknin, K. Kjaer, J. Als-Nielsen, and M. Lösche, Biophys. J. **59**, 1325 (1991).
[41] N. Nandi and B. Bagchi, J. Phys. Chem. A **101**, 1343 (1997).
[42] K.R. Mecke, Phys. Rev. E **53**, 4794 (1996).
[43] H.M. McConnell, P.A. Rice, and D.J. Bevegnu, J. Phys. Chem. **94**, 8965 (1990).
[44] D.J. Bevegnu and H.M. McConnell, J. Phys. Chem. **96**, 6820 (1992).
[45] S. Wurlitzer, P. Steffen, and T.M. Fischer, J. Chem. Phys. **112**, 5915 (2000).
[46] J. Als-Nielsen, D. Jacquemain, K. Kjaer, M. Lahav, F. Leveiller, and L. Leiserowitz, Phys. Rep. **246**, 251 (1994).
[47] V.M. Kaganer, G. Brezesinski, H. Möhwald, P.B. Howes, and K. Kjaer, Phys. Rev. E **59**, 2141 (1999).
[48] J.M. Kosterlitz and D.J. Thouless, J. Phys. (Paris) **6**, C1181 (1973).
[49] D.R. Nelson and B.I. Halperin, Phys. Rev. B **19**, 2457 (1979).
[50] V.M. Kaganer, H. Möhwald, and P. Dutta, Rev. Mod. Phys. **71**, 779 (1999).
[51] C.A. Helm, H. Möhwald, K. Kjaer, and J. Als-Nielsen, Biophys. J. **52**, 381 (1987).
[52] K. Kjaer, J. Als-Nielsen, C.A. Helm, P. Tippmann-Krayer, and H. Möhwald, Thin Solid Films **159**, 17 (1988).
[53] C.A. Helm, P. Tippmann-Krayer, H. Möhwald, J. Als-Nielsen, and K. Kjaer, Biophys. J. **60**, 1457 (1991).
[54] R.M. Kenn, K. Kjaer, and H. Möhwald, Colloids Surf., A **117**, 171 (1996).
[55] G. Brezesinski, A. Dietrich, B. Struth, C. Böhm, W.G. Bouwman, K. Kjaer, and H. Möhwald, Chem. Phys. Lipids **76**, 145 (1995).
[56] M. Lösche, H.-P. Duwe, and H. Möhwald, J. Colloid Interface Sci. **126**, 432 (1988).
[57] A. Miller, thesis, TU München, 1986.
[58] A. Miller and H. Möhwald, Europhys. Lett. **2**, 67 (1986).
[59] G. Brezesinski, A. Dietrich, B. Dobner, and H. Möhwald, Prog. Colloid Interface Sci. **98**, 255 (1995).
[60] K. R. Mecke (personal communication).